High-order spherical harmonics-nodal collocation scheme for the numerical solution of the time-dependent radiative transfer equation

MARÍA T. CAPILLA,* AND CÉSAR F. TALAVERA

Departamento de Matemática Aplicada. Universitat Politècnica de València. Camino de Vera 14. E-46022 Valencia, Spain.

*tcapilla@mat.upv.es

Abstract: The validity of the spherical harmonics-nodal collocation approximation to the stationary Boltzmann equation has been established in multi-dimensional neutron transport problems. This is a high-order approximation method that allows a coarse spatial discretization without losing accuracy. We extend the method to solve the time-dependent radiative transfer equation for absorbing media with anisotropic scattering, also incorporating to the model reflecting boundary conditions, due to the refractive index mismatching. The formalism is then applied to numerical test cases in one and two spatial dimensions that, using typical values in optical tomography for the physical parameters, check the accuracy and convergence of the method.

1. INTRODUCTION

The interest of the time-dependent radiative transfer equation has grown in recent years because of its applicability to a wide range of technological and research areas: nuclear reactions, combustion systems, astrophysics, short-pulsed laser systems, tomographic imaging using near-infrared light, and so on. Only for the very simplest problems it is possible to obtain exact analytical solutions [1]. Numerical solution methods are then required for realistic problems but, even with the capabilities of today's computers, a complete solution for a general scenario is still problematic.

Historically, the diffusion approximation to the radiative transfer equation is one of the most used methods due to its simplicity, easy implementation and robustness [2]. This approximation requires a medium where scattering is isotropic and dominates over the absorption. These conditions are not valid in many situations. For example, in optical tomography applied to biological tissues with small dimensions, high absorption or void-like areas [3], or with highly anisotropic scattering media.

Higher order approximation methods have then been developed to deal with more complex situations: multi-dimensional geometry, anisotropic scattering, variable physical properties, etc. Among the most used, we can cite the discrete ordinate (S_N) method [4, 5], the spherical harmonics (P_N) method [2, 6, 7] or the method of characteristics [8] for the angular dependence in the equation, and the finite-difference [9], finite-volume [5] or finite-element method [10, 11] for the spatial discretization (see for example, [3], for a compilation of recent numerical studies), and more recently meshfree methods [12]. Also, the integral formulation of the radiative transfer equation has been used in transient problems [13]. Finally, Monte Carlo methods are statistical models that can describe general geometries and properties but suffer from a high computational cost [14].

Advantages of the spherical harmonics method are that it can describe general geometries using spherical harmonics functions, and that the resulting equations preserve the symmetry under rotations of the transport equation (no ray effects). The method deals also, in a natural

way, with highly anisotropic scattering problems and highly focused external sources. Also, the resulting equations can be reformulated as diffusion-like partial differential equations, that are well established in numerical computation. A natural candidate for the approximation of the spatial variables is then a nodal collocation method [15], based on the use of orthonormal Legendre polynomials series, and developed by the authors in previous works [16, 17]. This method allows a discretization using coarse spatial rectangular nodes without losing accuracy in the results, thus reducing the size of the resulting numerical problem, in comparison with other methods as, for example, the finite difference method. Also, the resulting matrix of the corresponding algebraic problem is well-behaved and can be solved using standard numerical techniques.

Some limitations of the spherical harmonics-nodal collocation method are the ocassional appearance of oscillatory behavior, typical of the polynomial nature of the approximation, and the inability of the diffusion equation to deal with pure void zones, that must be replaced by void-like (with small but non zero coefficients) regions [17]. We finally mention that, to avoid the numerical complexities associated to a full P_N method, the simplified P_N (SP_N) approximation was proposed as a computational effective simplification of the P_N equations [18, 19], but has a limited range of applicability [20].

In the present work, the method is extended to obtain the solution of the time-dependent radiative transfer equation, as well as the treatment of boundary conditions between media with different refractive index. We also study the incorporation in our method of different types of external source, such as sources with highly anisotropic angular dependence or light pulse sources. We remark that, to our knowledge, this is the first time that this method has been extended to solve the time-dependent radiative transfer equation with semitransparent boundary conditions. For this reason, we systematically study the validity of the approximation, in a first stage, for stationary transfer problems with reflecting boundary conditions, and then for time-dependent transport problems with anisotropic scattering in absorbing media, for multi-dimensional geometries. We show that the method is well suited for the study of pulse transmission and reflection through media of optical properties with typical values in tomographic imaging of biological tissues.

The outline of the paper is as follows. In Section 2 we briefly describe the spherical harmonics approximation to the radiative transfer equation; the formalism is then applied to correctly describe Fresnel's reflecting boundary conditions under this approximation. The spatial discretization of the resulting problem is reviewed using a nodal collocation method established in previous works by the authors. In Section 3 the numerical accuracy and convergence of our method is validated with several stationary and time-dependent photon propagation problems. We study one and two-dimensional homogeneous cases, with refractive index mismatching at the boundaries and isotropic or anisotropic scattering. Also, in a one-dimensional case, the effect of an anisotropic incident source is analyzed. Other cases presented in this Section consist of two-dimensional heterogeneous tissue-like phantom with a void-like region, and a heterogeneous circular medium with an internal absorber region. Finally, in Section 4 we establish the main conclusions of this work and comment future works.

2. THE RADIATIVE TRANSFER EQUATION AND THE P_L EQUATIONS

2.1. The radiative transfer equation and boundary conditions

The interaction of thermal radiation with an absorbing and scattering medium is modelled by the radiative transfer equation (RTE). The photon intensity (or radiance) $I_\nu(\mathbf{r}, \boldsymbol{\omega}, t)$ of thermal radiation with fixed frequency ν, at location $\mathbf{r}$, traveling in the direction of the unitary vector $\boldsymbol{\omega} = \left(\sin\theta\,\cos\varphi,\ \sin\theta\,\sin\varphi,\ \cos\theta\right)$ (θ is the polar angle, φ is the azimuthal angle), at time t,

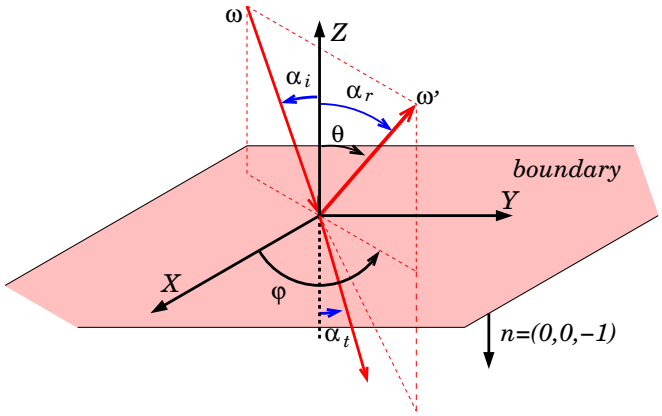

Fig. 1. Reflection and refraction angles and directions at the boundary between two different media. $\boldsymbol{\omega}'$ is the direction of the incident radiation, $\boldsymbol{\omega}$ and $\boldsymbol{\omega}''$ are the directions of the reflected and transmitted radiation, respectively.

for a non-emitting medium, is given by [2]

$$\frac{1}{c}\frac{\partial I_\nu}{\partial t}(\mathbf{r},\boldsymbol{\omega},t)+\boldsymbol{\omega}\cdot\nabla I_\nu(\mathbf{r},\boldsymbol{\omega},t)+(\mu_a+\mu_s)I_\nu(\mathbf{r},\boldsymbol{\omega},t)=\mu_s\int_{4\pi} I_\nu(\mathbf{r},\boldsymbol{\omega}',t)p(\boldsymbol{\omega},\boldsymbol{\omega}')\,d\Omega'+S(\mathbf{r},\boldsymbol{\omega},t)\,. \tag{1}$$

Here $d\Omega = \sin\theta\, d\theta d\varphi$, c is the speed of light in media, μ_a and μ_s are the absorption and scattering coefficients, p is the scattering phase function that describes the scattering directional probability and S is any internal source of radiation. For simplicity, we will omit the frequency subindex ν from now on.

The incoming radiative intensity at the boundary $\mathbf{r}_b$ of a medium with refractive index $n_m > n_0$ (n_0 is the vacuum refractive index that is taken as unity) is the sum of any external source and the partially reflected intensity

$$I(\mathbf{r}_b,\boldsymbol{\omega},t) = T(\mathbf{r}_b,\boldsymbol{\omega},t) + R(\boldsymbol{\omega}'\cdot\mathbf{n})\, I(\mathbf{r}_b,\boldsymbol{\omega}',t) \quad \text{for } \boldsymbol{\omega}\cdot\mathbf{n} < 0, \tag{2}$$

where (see Fig. 1) $\mathbf{n}$ is the outer normal vector to the boundary surface, $\boldsymbol{\omega}$ is the reflected direction, $\boldsymbol{\omega}' = \boldsymbol{\omega} - 2(\boldsymbol{\omega}\cdot\mathbf{n})\mathbf{n}$ is the direction of the incident radiation, $\alpha_r = -\boldsymbol{\omega}\cdot\mathbf{n}$ is the reflected angle, the incident angle $\alpha_i = \boldsymbol{\omega}\cdot\mathbf{n} = -\alpha_r$, the transmission angle α_t is given by Snell's law, $n_m \sin\alpha_i = n_0 \sin\alpha_t$, and finally R is the reflectivity, given by Fresnel's law: if $0 \le \alpha_r \le \alpha_c$ (α_c is the critical angle, $\sin\alpha_c = n_0/n_m$)

$$\begin{aligned} R &= \frac{1}{2}\left(\frac{n_m\cos\alpha_r - n_0\cos\alpha_t}{n_m\cos\alpha_r + n_0\cos\alpha_t}\right)^2 + \frac{1}{2}\left(\frac{n_m\cos\alpha_t - n_0\cos\alpha_r}{n_m\cos\alpha_t + n_0\cos\alpha_r}\right)^2 \\ &= \frac{1}{2}\left(\frac{n\sqrt{n^2\eta^2 - n^2 + 1} - \eta}{n\sqrt{n^2\eta^2 - n^2 + 1} + \eta}\right)^2 + \frac{1}{2}\left(\frac{n\eta - \sqrt{n^2\eta^2 - n^2 + 1}}{n\eta + \sqrt{n^2\eta^2 - n^2 + 1}}\right)^2, \end{aligned} \tag{3}$$

where $\eta = \cos\alpha_r \in [\eta_c, 1]$ with $\eta_c = \sqrt{1 - 1/n^2}$ and $n = n_m/n_0$; $R = 1$ otherwise: no transmission occurs when $\alpha_i > \alpha_c$ (or $0 \le \eta < \eta_c$).

The following quantities, of physical relevance, will be used in this work:

1. The incident radiation from all directions (fluence), at any instant of time,

$$\Phi(\mathbf{r},t) = \int_{4\pi} I(\mathbf{r},\boldsymbol{\omega},t)\, d\Omega\,. \tag{4}$$

2. The radiation received by a detector, outside the medium, with angular aperture given by transmitted angles in the range $|\alpha_t| < \alpha_t^{\max}$, and corresponding to incident angles at the boundary $|\alpha_i| < \alpha_i^{\max}$ with $\sin\alpha_i^{\max} = n_0/n_m \sin\alpha_t^{\max}$, is

$$\Phi_{\rm ap}(\mathbf{r}_b, t) = \int_{\Omega_{\rm ap}} [1 - R(\boldsymbol{\omega}\cdot\mathbf{n})] I(\mathbf{r}_b, \boldsymbol{\omega}, t)\, d\Omega\,. \tag{5}$$

3. The radiative heat flux (current) vector

$$\mathbf{J} = \int_{4\pi} I(\mathbf{r}, \boldsymbol{\omega}, t)\, \boldsymbol{\omega}\, d\Omega\,. \tag{6}$$

4. The outgoing radiative heat flux (current) onto a surface described by the normal outgoing vector $\mathbf{n}$

$$J_{\mathbf{n}}^{+} = \mathbf{J}\cdot\mathbf{n} = \int_{\boldsymbol{\omega}\cdot\mathbf{n}>0} I(\mathbf{r}, \boldsymbol{\omega}, t)\, \boldsymbol{\omega}\cdot\mathbf{n}\, d\Omega\,. \tag{7}$$

To numerically solve equation (1) we have first implemented the time discretization using some well-known numerical schemes: Forward-Euler, Backward-Euler and Crank-Nicolson. For each time step, we have extended in this work a numerical scheme, previously developed in [16, 17], that uses the spherical harmonics method for the angular dependence and a nodal collocation method for the spatial discretization of the equation.

2.2. The spherical harmonics approximation

To solve the RTE using a spherical harmonics approximation of finite order L, the angular dependence is replaced by a finite sum of spherical harmonics up to order L,

$$I(\mathbf{r}, \boldsymbol{\omega}, t) = \sum_{\substack{l=0 \\ -l\le m\le +l}}^{L} \phi_{lm}(\mathbf{r}, t) Y_l^m(\boldsymbol{\omega}), \qquad S(\mathbf{r}, \boldsymbol{\omega}, t) = \sum_{\substack{l=0 \\ -l\le m\le +l}}^{L} s_{lm}(\mathbf{r}, t) Y_l^m(\boldsymbol{\omega}), \tag{8}$$

where the spherical harmonics $Y_l^m(\boldsymbol{\omega}) = H_l^m P_l^m(\cos\theta)\exp(im\varphi)$, with constants $H_l^m = \sqrt{(2l+1)/(4\pi)}\sqrt{(l-m)!/(l+m)!}$ and $P_l^m(x)$ are the associated Legendre polynomials. In this work we will choose *odd* order L (see interface conditions later).

It is also assumed that the scattering angular probability p in Eq. (1) depends only on the relative angle between directions $\boldsymbol{\omega}$ and $\boldsymbol{\omega}'$. A common choice of phase function is the Henyey-Greenstein (HG) function [21]

$$p(\boldsymbol{\omega}\cdot\boldsymbol{\omega}') = \frac{1}{4\pi}\frac{1-g^2}{(1+g^2-2g\cos(\boldsymbol{\omega}\cdot\boldsymbol{\omega}'))^{3/2}}\,. \tag{9}$$

This choice has two advantages: the probability function depends on a unique parameter, the anisotropy factor $g \in [0, 1]$ (when $g = 0$ we have isotropic scattering), and it has a simple expansion in terms of Legendre polynomials $P_l(x)$, that is truncated to the same order as the spherical harmonics approximation,

$$p(\boldsymbol{\omega}\cdot\boldsymbol{\omega}') = \frac{1}{4\pi}\sum_{l=0}^{\infty}(2l+1)g^l P_l(\boldsymbol{\omega}\cdot\boldsymbol{\omega}') \simeq \frac{1}{4\pi}\sum_{l=0}^{L}(2l+1)g^l P_l(\boldsymbol{\omega}\cdot\boldsymbol{\omega}')\,. \tag{10}$$

Notice that, when g approaches 1 (highly anisotropic scattering media) a high order L is required to accurate approximate p. Then the scattering term in Eq. (1) can be written as

$$\mu_s \int_{4\pi} I(\mathbf{r}, \boldsymbol{\omega}', t) p(\boldsymbol{\omega}\cdot\boldsymbol{\omega}')\, d\Omega' = \sum_{l=0}^{L}\frac{1}{4\pi}\int_{4\pi} I(\mathbf{r}, \boldsymbol{\omega}', t)(2l+1)\mu_{s,l}P_l(\boldsymbol{\omega}\cdot\boldsymbol{\omega}')\, d\Omega',$$

where $\mu_{s,l} = \mu_s g^l$, $l = 0, 1, \ldots$, are the scattering coefficients.

We will also impose that the solutions of the spherical harmonics method must be real functions, that is, $I = I^*$ (the star denotes complex conjugation). This implies the constrains on the coefficients of the finite expansion $\phi^*_{lm} = (-1)^m \phi_{l,-m}$ and so there are $2l + 1$ real unknowns, denoted as $\{\xi_{l0} = \phi_{l0}\,, \xi_{lm} = \mathrm{Re}\,\phi_{lm} = \frac{1}{2}(\phi_{lm} + (-1)^m \phi_{l,-m}), \eta_{l,m} = \mathrm{Im}\,\phi_{lm} = \frac{1}{2i}(\phi_{lm} - (-1)^m \phi_{l,-m}), m = 1, \ldots, l\}$, for each $l = 0, 1, \ldots, L$.

To simplify the exposition of the method, we will consider in the following the stationary RTE. The introduction of the (classical) time discretization schemes can be carried out following the same steps, with appropriate changes on the matrices Σ_a, $\bar{\Sigma}_a$ and source term S, $\bar{S}$. If we replace expansions (8) and (10) into the RTE (1) and make use of the orthonormality properties of the spherical harmonics, we obtain a set of $2l + 1$ first order real differential equations that can be written [17] in vector form as

$$\sum_{j=1}^{3} M_j \frac{\partial \bar{X}}{\partial x_j} + \Sigma_a X = \mathcal{S}\,, \qquad \sum_{j=1}^{3} \bar{M}_j \frac{\partial X}{\partial x_j} + \bar{\Sigma}_a \bar{X} = \bar{\mathcal{S}}\,, \tag{11}$$

where we have conveniently gather the unknowns into the vector of even index l $X = (\xi_{l,m\geq 0},\, \eta_{l,m>0})_{l\,=\mathrm{even}}$ and the vector of odd index l $\bar{X} = (\xi_{l,m\geq 0},\, \eta_{l,m>0})_{l\,=\mathrm{odd}}$, and analogously with the source term $\mathcal{S} = (\mathrm{Re}\, s_{l,m\geq 0},\, \mathrm{Im}\, s_{l,m>0})_{l\,=\mathrm{even}}$, $\bar{\mathcal{S}} = (\mathrm{Re}\, s_{l,m\geq 0},\, \mathrm{Im}\, s_{l,m>0})_{l\,=\mathrm{odd}}$. The rectangular matrices M_j and $\bar{M}_j$ contain the numerical factors arising from the orthonormality properties of the spherical harmonics. Finally, the square diagonal matrices $\Sigma_a = \mathrm{diag}(\mu_a + \mu_s - \mu_{s,l})_{l\,=\mathrm{even}}$ and $\bar{\Sigma}_a = \mathrm{diag}(\mu_a + \mu_s - \mu_{s,l})_{l\,=\mathrm{odd}}$ contain the physical coefficients of the medium.

If $\bar{\Sigma}_a$ is non-singular, we can write $\bar{X}$ in terms of X using the second equation of (11)

$$\bar{X} = -D \sum_{j=1}^{3} \bar{M}_j \frac{\partial X}{\partial x_j} + D\,\bar{\mathcal{S}}\,, \tag{12}$$

where $D = \bar{\Sigma}_a^{-1}$. Inserting Eq. (12) into the first equation (11), a second-order vector-valued differential equation is obtained:

$$-\sum_{i,j=1}^{3} \frac{\partial}{\partial x_i}\left(M_i D \bar{M}_j \frac{\partial X}{\partial x_j}\right) + \Sigma_a\, X = \mathcal{S} - \sum_{j=1}^{3} \frac{\partial}{\partial x_j}(M_j D \bar{\mathcal{S}})\,. \tag{13}$$

This equation is the diffusive form of P_L equations, for a multi-dimensional spatial geometry. Some simplifications are possible when the medium has a particular symmetry:

1. If the physical properties of the medium are independent of the Z direction, the intensity I must obey the constraints $\frac{\partial I}{\partial z} = 0$ and $I(\theta) = I(\pi - \theta)$ (θ is the polar angle); this implies that the coefficients $\phi_{lm} = 0$ when $l + m$ is odd.

2. In planar geometry approximation, the medium is infinite in the XY plane and the coefficients depend only on the Z direction; the only dependence of the intensity is then $I = I(z, \theta)$ and the only nonzero coefficients are $\phi_{l,0}$ and they are real.

Eqs. (11) require some *interface conditions* at points of discontinuity (of the coefficients or the source). A natural approach [22] comes from replacing the discontinuity with a very thin transition region, of thickness $\Delta > 0$, where the physical properties change in a continuous way. If, for example, the discontinuity occurs at the YZ plane, integrating Eqs. (11) over the transition region and taking $\Delta \to 0+$ we arrive at the *interface conditions* [17]

$$\lim_{\Delta\to 0+} M_1 \bar{X}(x + \Delta) = \lim_{\Delta\to 0+} M_1 \bar{X}(x - \Delta), \qquad \lim_{\Delta\to 0+} \bar{M}_1 X(x + \Delta) = \lim_{\Delta\to 0+} \bar{M}_1 X(x - \Delta)\,. \tag{14}$$

If the approximation order L is *odd*, then the rectangular matrix $\bar{M}_1$ has maximum rank and the second condition implies continuity of all coefficients X of even index l; this is not true for the first condition and it is not possible to guarantee continuity of all coefficients $\bar{X}$ with odd index l.

According to the expansion (8), the incident radiation or fluence (4) is the first coefficient of the spherical harmonics expansion, $\Phi(\mathbf{r},t) = \sqrt{4\pi}\,\phi_{00}$, and, given that $\boldsymbol{\omega} = \big(\sqrt{2\pi/3}\,(Y_1^{-1} - Y_1^1),\ i\sqrt{2\pi/3}\,(Y_1^{-1} + Y_1^1),\ 2\sqrt{\pi/3}\,Y_1^0\big)$, the radiative heat flux vector (6) is

$$\mathbf{J} = \left(\sqrt{\frac{2\pi}{3}}(\phi_{1,-1} - \phi_{1,1}),\ i\sqrt{\frac{2\pi}{3}}(\phi_{1,-1} + \phi_{1,1}),\ \sqrt{\frac{4\pi}{3}}\phi_{1,0}\right) = -2\sqrt{\frac{2\pi}{3}}\left(\xi_{11},\ \eta_{11},\ \frac{-1}{\sqrt{2}}\,\xi_{10}\right), \quad (15)$$

where we have used the real condition $\phi_{l,-m} = (-1)^m \phi_{l,m}^*$ ($\xi_{lm} = \mathrm{Re}\,\phi_{l,m}$, $\eta_{lm} = \mathrm{Im}\,\phi_{l,m}$). In the particular case of symmetry along the Z direction, the coefficients with indices $l + m$ odd are zero, and then $\mathbf{J} = -2\sqrt{2\pi/3}\big(\xi_{11},\ \eta_{11},\ 0\big)$. The transmitted radiation that arrives to a detector with angular aperture $|\alpha_t| < \alpha_t^{\max}$ is, to finite order L,

$$\begin{aligned}\Phi_{\mathrm{ap}}(\mathbf{r}_b,t) &= \int_{\Omega_{\mathrm{ap}}} [1 - R(\boldsymbol{\omega}\cdot\mathbf{n})] \sum_{l=0,|m|\le l}^{L} \phi_{lm}(\mathbf{r}_b,t) Y_l^m(\boldsymbol{\omega})\, d\Omega \\ &= \sum_{l=0}^{L}\left[\xi_{l0}(\mathbf{r}_b,t)\, H_l^0\, \mathcal{I}_c(l,0) + \sum_{m=1}^{l}\left\{\xi_{lm}(\mathbf{r}_b,t)\, 2H_l^m\, \mathcal{I}_c(l,m) - \eta_{lm}(\mathbf{r}_b,t)\, 2H_l^m\, \mathcal{I}_s(l,m)\right\}\right], \quad (16)\end{aligned}$$

where $\mathcal{I}_{c,s}(l,m) = \int_{\Omega_{\mathrm{ap}}} [1 - R(\alpha_t)] \begin{Bmatrix}\cos(m\varphi)\\ \sin(m\varphi)\end{Bmatrix} P_l^m(\theta)\, d\Omega$. For the computation of these integrals, see Appendix A.

2.3. Approximation of boundary conditions

Boundary conditions (2) require an approximate description when a finite spherical harmonics expansion is used. A popular choice is given by Marshak's conditions [23], where integration of l odd coefficients, for incoming angular directions, vanish in Eq. (2)

$$\int_{\boldsymbol{\omega}\cdot\mathbf{n}\le 0} Y_l^m(\boldsymbol{\omega})^* [I(\mathbf{r}_b,\boldsymbol{\omega},t) - T(\mathbf{r}_b,\boldsymbol{\omega},t) - R(\boldsymbol{\omega}'\cdot\mathbf{n}) I(\mathbf{r}_b,\boldsymbol{\omega}',t)] d\Omega = 0, \quad (17)$$

for $l = 1, 3, \ldots, L$ (odd) and $m = 0, 1, \ldots, l$ (no additional constraints are obtained for $m < 0$ because of the real condition $\phi_{lm}^* = (-1)^m \phi_{l,-m}$). If the external source T is approximated by a finite order spherical harmonics expansion,

$$T(\mathbf{r}_b,\boldsymbol{\omega},t) = \sum_{\substack{l=0\\ -l\le m\le +l}}^{L} T_{lm}(\mathbf{r}_b,t) Y_l^m(\boldsymbol{\omega}), \quad (18)$$

and using Eqs. (8) and the fact that, for prismatic geometry $\int_{\boldsymbol{\omega}\cdot\mathbf{n}\le 0} Y_l^{m*}(\boldsymbol{\omega}) Y_{l'}^{m'}(\boldsymbol{\omega})\, d\Omega = \frac{1}{2}\delta_{ll'}\delta_{mm'}$ when $l + l'$ is odd, we obtain that Marshak's conditions (17) can be rewritten, for $l = 1, 3, \ldots, L$ odd and $m = 0, 1, \ldots, l$, as (from now on we omit the independent variables)

$$\phi_{lm} - T_{lm} + \sum_{\substack{l' \text{ even}\\ |m'|\le l'}}^{L-1} N^V_{lm,lm'}\,(\phi_{l'm'} - T_{l'm'}) - \sum_{\substack{l'=0\\ |m'|\le l'}}^{L} N^R_{lm,l'm'}\,\phi_{l'm} = 0, \quad (19)$$

where the integrals

$$N^V_{lm,l'm'} = 2\int_{\boldsymbol{\omega}\cdot n\le 0} Y_l^{m*}(\boldsymbol{\omega}) Y_{l'}^{m'}(\boldsymbol{\omega})\, d\Omega, \tag{20}$$

$$N^R_{lm,l'm'} = 2\int_{\boldsymbol{\omega}\cdot \mathbf{n}\le 0} Y_l^{m*}(\boldsymbol{\omega}) R(\boldsymbol{\omega}\cdot\mathbf{n}) Y_{l'}^{m'}(\boldsymbol{\omega})\, d\Omega. \tag{21}$$

The explicit form of these integrals depends on the orientation of the boundary surface. See [17] for the evaluation of N^V. With respect to N^R if, for example, the outer normal vector to the boundary surface points to negative Z-axis, $\mathbf{n} = (0, 0, -1)$, the reflected angle $\cos\alpha_r = \cos\theta$ is the polar angle, the reflected direction $\boldsymbol{\omega}'$ corresponds to angles $(\varphi, \pi - \theta)$ and, if we define $\eta = \cos\theta$, then

$$N^{R,3-}_{lm,l'm'} = 4\pi\delta_{mm'} H_l^m H_{l'}^{m'} (-1)^{l'+m'} \int_0^1 P_l^m(\eta) R(\eta) P_{l'}^m(\eta)\, d\eta, \tag{22}$$

for $l = 1, 3, \ldots, L$ odd and $m = 0, 1, \ldots, l$. The remaining integrals are then numerically evaluated [24].

It is convenient to write Eq. (19) in vector form

$$(\mathbb{I} - \bar{N}^R)\cdot \bar{X} + (N^V - N^R)\cdot X = \bar{T} + N^V \cdot T, \tag{23}$$

where $\mathbb{I}$ is the identity matrix, the vectors $T = (T_{lm})_{l=\text{even}}$, $\bar{T} = (T_{lm})_{l=\text{odd}}$ and the matrices $N^R = (N^R_{lm,l'm'})_{l'=\text{even}}$, $\bar{N}^R = (N^R_{lm,l'm'})_{l'=\text{odd}}$. Notice that, when $n_m = n_0$, then $N^R = \bar{N}^R = 0$ and Eq. (23) reduces to Marshak's vacuum boundary condition [17]. It can be shown that, for the three Cartesian axes, the following relationship between positive and negative axis holds for these matrices: $N^{V,+} = -N^{V,-}$ and $N^{R,+} = -N^{R,+}$; $\bar{N}^{R,+} = +\bar{N}^{R,-}$. We finally notice that at the discontinuity given by the boundary the analogous of the interface conditions given by Eqs. (14) are introduced. Using then Eq. (12) we obtain the same coupling equations for X fields that for interior nodes, the only difference being the coupling coefficients [17].

2.4. The nodal collocation method

Equation (13) is a diffusion type equation, and can be effectively approximated by a nodal collocation method, that allows good accuracy using a coarse spatial discretization. A detailed description of the development of the method can be found in [15] and [25], where the method was applied to the neutron diffusion equation, and in [16, 17], where the method was generalized to P_L equations of arbitrary odd order L and multi-dimensional rectangular geometries.

If we assume that the spatial domain can be described by a set of N adjacent rectangular prisms or nodes, of an structured rectilinear mesh with vertex coordinates (in Cartesian coordinates) $\{x_{1,i_1}, x_{2,i_2}, x_{3,i_3}\}$ where i_j are the vertex indices, the nodal collocation method is based on the following assumptions: i) the physical properties of Eq. (1) are constant on each spatial node, and ii) the spatial dependence on each node is approximated by a finite expansion in terms of orthonormal Legendre polynomials. Then,

1. Each spatial node $N^e = [x_{1,i_1}, x_{1,i_1+1}] \times [x_{2,i_2}, x_{2,i_2+1}] \times [x_{3,i_3}, x_{3,i_3+1}]$, with $e = 1, \ldots, N$ the node index, is scaled to the canonical cube $N^3_u = [-\frac{1}{2}, \frac{1}{2}]^3$ using the change of variable $u_j = [x_j - \frac{1}{2}(x_{j,i_j} + x_{j,i_j+1})]/\Delta x^e_j$, with $\Delta x^e_j = x_{j,i_j+1} - x_{j,i_j}$, for each spatial coordinate.

2. This change of variable is also applied to Eq. (13) and the vector solution $X^e(\mathbf{u})$, where $\mathbf{u} = (u_1, u_2, u_3)$, of Eq. (13) on node N^e_u is replaced by a finite sum of orthonormal Legendre polynomials $\mathcal{P}_k(u) = \sqrt{2k+1}\, P_k(2u)$, $-\frac{1}{2} < u < \frac{1}{2}$. In terms of the new variable,

$$X^e(\mathbf{u}) = \sum_{k_1,k_2,k_3=0}^{M} x^e_{k_1,k_2,k_3} \prod_{j=1}^{3} \mathcal{P}_{k_j}(u_j), \tag{24}$$

where M is the spatial expansion order.

The truncated series (24) is then inserted into Eq. (13); then, using the orthonormality properties of the Legendre polynomials $\mathcal{P}_k(u)$, the interface conditions (14) for adjacent nodes and the boundary conditions (23), Eq. (13) is reduced to a linear system for the unknown coefficients $x^e_{k_1,k_2,k_3}$ (see [17] for explicit computations). The matrix of the resulting system is large, sparse, real and non-symmetric, and the dimension of the system depends on the number of spatial nodes N, the order M of the Legendre expansion (24) and the order L of the spherical harmonics approximation.

3. NUMERICAL RESULTS

In this Section, the numerical approach described above is applied to different light propagation models. The numerical methods were implemented into the FORTRAN 90 code SHNC, for arbitrary P_L approximation with L odd, arbitrary Legendre order M, and multi-dimensional geometry. The linear system is iteratively solved using SPARSKIT's implementation [26] of the biconjugate gradient stabilized method BCGSTAB with incomplete LU factorization as preconditioner. For very large systems, parallel computations can be performed using PETSc [27] BCGSTAT method and HYPRE BoomerAMG as parallel preconditioner. The time interval can be splitted into time zones where all physical properties of the RTE (1) can be different. In our computations, we have taken a uniform time step for each time zone.

The SHNC code was developed initially for neutron transport problems [16, 17], and later adapted to solve external fixed source stationary problems in the field of optical tomography [28]. In this work, we have incorporated the time evolution and the treatment of semitransparent boundary conditions between media with different refractive index and optical properties. We test the application of the numerical method to light propagation models by choosing a set of appropriate numerical problems.

This Section consists of three parts. In the first part, we present results of several P_L approximations of the steady-state and the time-dependent forms of the RTE for one-dimensional homogeneous slabs, considered as academic tests, and we compare these results with reference solutions. In the second part, we compare the numerical results with experimental measurements for the 2D homogeneous and heterogeneous tissue models described in [29]. Finally, in the third part of this Section, time-dependent P_L results are presented for a heterogeneous circular medium, described in [11]. We study the influence on the transport of photons through this medium when the absorption in one of the regions is changed. In this last case, we will describe the performance of our method, since it requires more computational resources. When appropriate, time evolution has been carried out numerically using Crank-Nicolson scheme, with constant step size in each time zone. This method, in our numerical test, allows us to efficiently obtain accurate results using large time steps, with similar computational requirements as Backward-Euler method.

3.1. Validation of the numerical scheme in one-dimensional slabs

3.1.1. Homogeneous medium with refractive index

This academic steady-state problem allows as to validate the reflective boundary conditions and to introduce the approximation to the external source as an even or odd function with corresponding normalization condition. These ideas will be used in successive tests. Furthermore, the physical parameters are chosen far from difussive regime and finally, the existence of analytic solution allows us to verify the convergence of the P_L results.

The one-dimensional time-independent radiative transport equation for planar geometry in a transversely infinite medium (the XY plane) with no scattering is given by

$$(\eta\partial_z + \mu_a)\, I(z,\eta) = S(z,\eta), \quad 0 < z < l\,,\ -1 \le \eta \le +1\,, \tag{25}$$

where $I(z,\eta)$ is the photon intensity and $\eta = \cos\theta \in [-1,1]$, being θ the polar angle. In this case the internal light source is $S(z,\eta) = 0$. The isotropic external source as incoming radiance at the left boundary is $T(0,\eta)$, and vacuum boundary condition is applied at the right side of the medium ($z = l$). Also, the refractive index mismatching is considered at the boundaries, then the boundary condition (2) is given by

$$\begin{aligned} I(0,\eta) &= T(0,\eta) + R(\eta) I(0,-\eta), \quad \text{if } 0 < \eta \le +1, \\ I(l,\eta) &= R(-\eta) I(l,-\eta), \qquad \text{if } -1 \le \eta < 0, \end{aligned} \tag{26}$$

where $R(\eta)$ is the reflectivity (3). By imposing the boundary condition (26), we obtain the analytical solution of the RTE for this particular test case:

$$I(z,\eta) = \begin{cases} T(0,\eta)\, \frac{1}{1-R^2(\eta)\exp\left[-2\frac{\mu_t}{\eta} l\right]} \exp\left[-\frac{\mu_t}{\eta} z\right] & \text{if } 0 < \eta \le +1, \\ T(0,-\eta)\, \frac{R(-\eta)}{1-R^2(-\eta)\exp\left[2\frac{\mu_t}{\eta} l\right]} \exp\left[-\frac{\mu_t}{\eta}(z-2l)\right] & \text{if } -1 \le \eta < 0\ . \end{cases} \tag{27}$$

The isotropic photon intensity (fluence) for planar geometry is given by

$$\Phi(z) = \int_{-1}^{+1} I(z,\eta)\, d\eta = \int_0^{+1} T(0,\eta)\, \frac{\exp\left[-\frac{\mu_t}{\eta} z\right] + R(\eta)\, \exp\left[\frac{\mu_t}{\eta}(z-2l)\right]}{1 - R^2(\eta)\, \exp\left[-2\frac{\mu_t}{\eta} l\right]}\, d\eta\,. \tag{28}$$

We will use dimensionless units in the parameters of this problem. A slab of length $l = 1$ is considered, we choose $\mu_a = 1$ (far from the diffusive regime, where $\mu_s \gg \mu_a$), the refractive index $n_m = 1.4$ and an isotropic external source $T(0,\eta) = T = 1$, $\eta \in]0,1]$.

The approximation of the external source T by a finite sum of spherical harmonics in Eq. (18) reduces, in the planar geometry (where all coefficients with index $m \neq 0$ are null), to a finite development in Legendre polynomials,

$$T(0,\eta) \simeq \sum_{l=0}^{L} T_l \sqrt{\frac{2l+1}{4\pi}}\, P_l(\eta), \tag{29}$$

where the coefficients are $T_l = T_{l,m=0} = \sqrt{4\pi}\sqrt{2l+1}\, 1/2 \int_{-1}^{1} T(0,\eta) P_l(\eta)\, d\eta$, $l = 0, 1, \ldots$.

We will also introduce a normalization condition: the incoming photon intensity from the external source must be equal to that from the finite approximation. That is,

$$\int_0^1 T(0,\eta)\, d\eta = \int_0^1 \sum_{l=0}^{L} T_l \sqrt{\frac{2l+1}{4\pi}}\, P_l(\eta)\, d\eta = T_0 \frac{1}{\sqrt{4\pi}} + \sum_{l=1,3\ldots}^{L} T_l \sqrt{\frac{2l+1}{4\pi}} \frac{1}{l+1} P_{l-1}(0), \tag{30}$$

where in the last line we have used that $\int_0^1 P_0(\eta)\, d\eta = 1$; $\int_0^1 P_l(\eta)\, d\eta = 1/(l+1) P_{l-1}(0)$ for $l = 1, 2, \ldots$ (and the recurrence relation $(2l+1)P_l(x) = \frac{d}{dx}(P_{l+1}(x) - P_{l-1}(x))$) and finally that $P_l(0) = 0$ for $l =$ odd (see recurrences (38)).

Notice that boundary conditions are set for incoming directions (in this case, for $\eta \in [0,1]$). If we define the external source as an *even* function $T(-\eta) = T(+\eta)$, then

$$T(0,\eta) = \sum_{l\ =\text{even}}^{L} T_l \sqrt{\frac{2l+1}{4\pi}}\, P_l(\eta), \tag{31}$$

with $T_{l\ =\text{even}} = \sqrt{4\pi}\sqrt{2l+1} \int_0^1 T(0,\eta) P_l(\eta)\, d\eta$ and $T_{l\ =\text{odd}} = 0$. In particular, for an isotropic source, $T_l = \sqrt{4\pi}\, \delta_{l0}\, T(0)$, and the normalization condition (30) is trivially satisfied.

The photon intensity is calculated with the numerical P_L approximations using the SHNC code, with a mesh consisting of 10 nodes with size $\Delta z = 0.1$. The order M used in the Legendre polynomials expansion (24) is $M = 4$. Fig. 2 shows the photon intensity (28) as a function of the distance z from the source. The P_L solutions for $L = 1, 3, 5, 7$, are compared to the analytical solution (28), obtained by numerical integration using QUADPACK [24]. The P_1 approximation

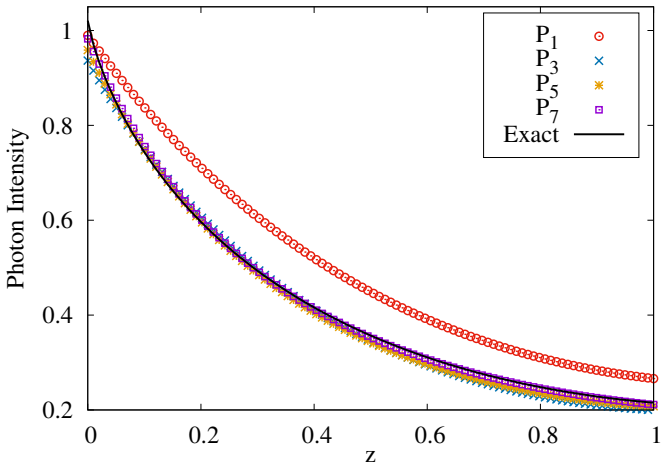

Fig. 2. Photon intensities for the homogeneous one-dimensional problem.

can not reproduce the exact solution of the intensity, while the P_3, P_5 and P_7 solutions are very close to the exact solution. The P_7 approximation tests the convergence of our method. The optical properties considered make the medium far from a diffusive regime, this explains the discrepancy between the P_1 approximation and high order P_L.

3.1.2. Time evolution for a medium with a highly anisotropic incident radiation

This test case will validate the behavior of the method for a time-dependent RTE when a source with strong angular dependence is applied to the boundary, and we will also verify the positivity of the numerical solution.

The configuration of this problem is the same as the one described above, but now the external source applied at the left boundary is the mono-directional incident radiation given by a delta function, $T(0, \eta) = T\,\delta(\eta - 1)$, with $T = 100$ and $\eta = \cos\theta \in [0, 1]$ (as in test of Section 3.1.1, we now also use dimensionless units in all parameters). Vacuum condition is considered at the right side of the medium. This case is based on the examples presented in [30]. The length of the slab is $l = 1$, and we consider now $\mu_a = 0.5$ and $\mu_s = 5$ ($\mu_a \ll \mu_s$). The time-dependent P_L solutions of the RTE will be compared with S_{48} results obtained with the transport code PARTISN [31], which solves the multigroup discrete ordinates form of the Boltzmann transport equation. The S_{48} results are taken as reference solutions.

We simulate numerically the δ function by a Gaussian of width $\epsilon = 0.1$ for incoming directions, $T(0, \eta) \simeq T' \exp[-(\eta - 1)^2/\epsilon^2]$, $\eta \in [0, 1]$, where the constant $T' = T/(\epsilon\sqrt{\pi}/2\,\mathrm{erf}(\epsilon^{-1}))$ ($\mathrm{erf}(x)$ is the error function) is such that the external source preserves the incoming photon intensity:

$$\int_0^1 \delta(\eta - 1)\, d\eta = \frac{1}{\epsilon\frac{\sqrt{\pi}}{2}\,\mathrm{erf}(\epsilon^{-1})} \int_0^1 \exp\left[-\frac{(\eta - 1)^2}{\epsilon^2}\right] d\eta\,. \tag{32}$$

Before performing this development, we extend the Gaussian to be an *odd* function in the interval $[-1, 1]$, $T(-\eta) = -T(\eta)\ \forall\eta$ (therefore half of the coefficients in the Legendre expansion are

required; also, an odd function gives a better approximation to the external source for P_1 equations than an even function, that consists of a horizontal line). The finite order approximation (29) is

$$T(0,\eta) = \sum_{l\,=\text{odd}}^{L} T_l \sqrt{\frac{2l+1}{4\pi}}\, P_l(\eta), \tag{33}$$

with coefficients $T_{l\,=\text{even}} = 0$ and $T_{l\,=\text{odd}} = \sqrt{4\pi}\sqrt{2l+1}\,T''\,\mathcal{I}_l$, where $\mathcal{I}_l = \int_0^1 \exp[-(\eta - 1)^2/\epsilon^2] P_l(\eta)\,d\eta$. These integrals can be computed recursively, see Appendix B. The value of the constant T'' is obtained from the normalization condition (30):

$$\int_0^1 T\,\delta(\eta-1)\,d\eta = T = T'' \sum_{l=1,3,\ldots}^{L} \frac{2l+1}{l+1}\,\mathcal{I}_l\,P_{l-1}(0)\,. \tag{34}$$

In Fig. 3 we show the P_1, P_7 and S_{48} solutions at times $t = 0.1$ and $t = 1.0$. The SHNC P_L solutions have been calculated using the same mesh discretization and Legendre polynomial order M as the previous 1D test. We take nodes of length $\Delta z = 0.1$ to guarantee that no negative values of the solution are obtained. If $\Delta z = 0.2$ is considered, the P_1 solution at $t = 0.1$ has unphysical negative values.

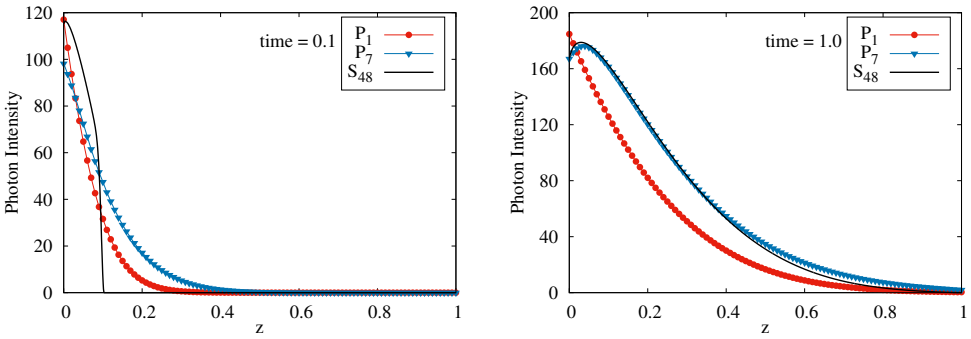

Fig. 3. Homogeneous 1D problem with anisotropic incident radiation at times (a) $t = 0.1$ and (b) $t = 1.0$.

At time $t = 1.0$, in Fig. 3(b), we observe good agreement between P_7 and S_{48} solutions. The discrepancy between the P_1 solution and the P_7 and S_{48} solutions in Fig. 3(b) is due to the strong angular dependence of the source, then the P_1 approximation is not able to describe the transport of photons through this medium. We have verified that the P_7 approximation is enough to reproduce the reference solution for this problem. The behavior of the numerical solution for small times (Fig. 3(a)) is typical of the approximation of discontinuous initial conditions at the left boundary by continuous functions [30]. The mean free path for this problem is $(\mu_a + \mu_s)^{-1} \simeq 0.2$, and it gives us a time scale (we have taken $c = 1$): for $t > 0.2$ the accuracy of the P_7 approximation improves and it converges quickly to the S_{48} reference solution. When we approach the steady state of the system ($t \simeq 5$), P_7 and S_{48} solutions coincide, remaining a small discrepancy of less than 2.5% in the vicinity of the source ($z \simeq 0.01$).

3.2. *Two-dimensional tissue phantoms and experimental validation*

To test our numerical method dealing with two-dimensional problems, in this Section we study the homogeneous and heterogeneous tissue-phantoms studied by Klose et al in [29]. The goal is

to test the SHNC P_L solutions with experimental measurements; this study constitutes the first experimental validation of our numerical method applied to 2D photon transport problems. We also verify that our method is able to achieve accurate results using a coarse spatial mesh thus reducing the memory storage required for the computation.

The experimental setup of these models is described in [29], where the reader can consult details about the composition of the phantoms and the adjustment of the optical properties of the materials. The numerical calculations presented in two dimensions correspond to a thin slice of the three-dimensional configurations, that is described by a two-dimensional RTE with angular dependence only on the azimuthal angle. Also, in [29] the upwind-difference discrete-ordinates algorithm is used to approximate the solution of the RTE for these cases.

3.2.1. 2D homogeneous phantom I

The first two-dimensional homogeneous medium considered in this work is a 3 cm × 3 cm square, named as *phantom I*. The system is illuminated by a 678 nm-light continuous wave source with a width of 0.1 cm, placed at different locations along the bottom boundary. The refractive index of the phantom material is $n_m = 1.56$.

Our numerical method is now tested comparing the P_L predictions of the transmitted photon intensity at different detector positions with the corresponding experimental data extracted from Fig. 2 of [29]. The external source of unit magnitude is located at three different locations along the X-axis: source A at $x = 1.5$ cm; source B at $x = 0.9$ cm and source C at $x = 0.3$ cm. In Fig. 4 (left), we show the geometry and dimensions of phantom I. For the numerical calculations we consider a non-uniform grid mesh of 17 × 15 nodes; in the vicinity of the source position, we have adapted the distance between nodes to obtain a source with a width of 0.1 cm. The grid is schematically described in Fig. 4 (a) for the source A.

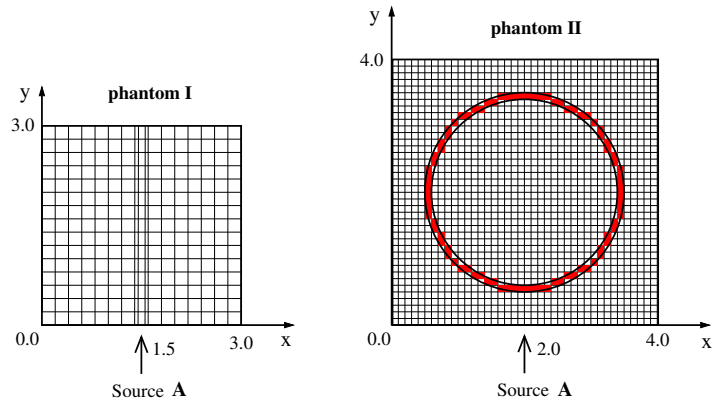

Fig. 4. Geometry and spatial discretization of 2D problems. Left: phantom I, with 17 × 15 nodes. Right: phantom II, with 40 × 40 nodes. Units are in cm.

We have investigated the sensitivity of the numerical P_9 results when the optical parameters are varied. We have evaluated for a set of cases the average error between our numerical results and the experimental measurements, given by $E = 100/N\sqrt{\sum_{i=1}^{N}(M_i - I_i)^2/M_i^2}$, where M_i are the experimental data, I_i the P_9 results and $N = 28$ the number of detected measurements [29].

In Table 1, we show the values of E by summing the readings of the detectors along the top side of the medium ($0 \leq x \leq 3$ cm, $y = 3$ cm) and the left side ($x = 0$ cm, $0 \leq y \leq 3$ cm), for each source position. The Table shows results obtained for different values of μ_s (or μ_a) when μ_a and g (or μ_s and g) are kept constant. The last case in the Table corresponds to the cases of fixed μ_a and μ_s but varying the scattering degree of anisotropy g. In the case when the reduced

scattering coefficient μ_s' is fixed, we have observed the known fact that the error oscillates very slightly when varying the values of μ_s and g.

Table 1. Average error E between the calculated P_9 and the measured normalized photon intensities along the top and the left sides of phantom I. The error is evaluated for different source positions and varying the optical parameters

	Top side (X-axis, $y = 3$ cm)			Left side (Y-axis, $x = 0$ cm)		
	Source A	Source B	Source C	Source A	Source B	Source C
μ_s' (cm^{-1})	($\mu_a = 0.175$ cm^{-1}, $g = 0.8$)					
2.9	1.33	2.61	2.91	3.29	6.14	22.69
4.35	0.45	1.65	1.62	0.77	0.69	4.81
5.8	0.85	1.37	1.19	2.43	3.18	3.05
8.7	1.79	1.93	2.21	5.25	7.04	9.21
11.6	2.42	2.68	3.41	7.07	9.16	11.81
μ_a (cm^{-1})	($\mu_s = 29$ cm^{-1}, $g = 0.8$)					
0.05	0.64	3.32	4.94	7.27	10.33	19.42
0.1	0.71	2.38	3.09	2.81	3.06	6.53
0.175	0.85	1.37	1.19	2.43	3.18	3.05
0.25	1.03	1.13	1.69	5.13	6.65	7.50
0.35	1.32	1.84	3.49	7.63	9.41	10.68
g	($\mu_s = 29$ cm^{-1}, $\mu_a = 0.175$ cm^{-1})					
0.7	1.79	1.93	2.21	5.27	7.06	9.19
0.75	1.37	1.57	1.58	4.02	5.45	6.86
0.8	0.85	1.37	1.19	2.43	3.18	3.05
0.85	0.45	1.66	1.65	0.80	0.68	4.71
0.9	1.32	2.64	2.98	3.45	6.29	21.98

For the SHNC P_L calculations in Figs. 5 and 6 we consider the scattering coefficient $\mu_s = 29$ cm^{-1} and the absorption coefficient $\mu_a = 0.175$ cm^{-1}. The anisotropy factor is $g = 0.8$ and the reduced scattering $\mu_s' = 5.8$ cm^{-1}. This choice corresponds to one of the most favorable cases in Table 1. The convergence of the P_L approximations for source A along $0 \le x \le 15$ mm for $y = 30$ mm, and along $0 \le y \le 15$ mm for $x = 0$ mm is shown in Figs. 5(a) and 5(b), respectively. We observe a small oscillatory behavior for low order P_L near the corners that is damped when the order L increases.

In Fig. 6, we show numerical solutions for each source position, obtained along the top side (Fig. 6 (a)) and the left side (Fig. 6 (b)) of the medium. The P_1 and P_9 solutions of the steady state photon intensity are compared in Fig. 6 with 28 experimental measurements in each side [29], normalized by their mean value. We have verified that it is not necessary to take a finer mesh to obtain accurate results, since considering 60×60 nodes, the P_L results of Fig. 6 remain unchanged. Our results are compatible with [29] if we take into account that the theoretical

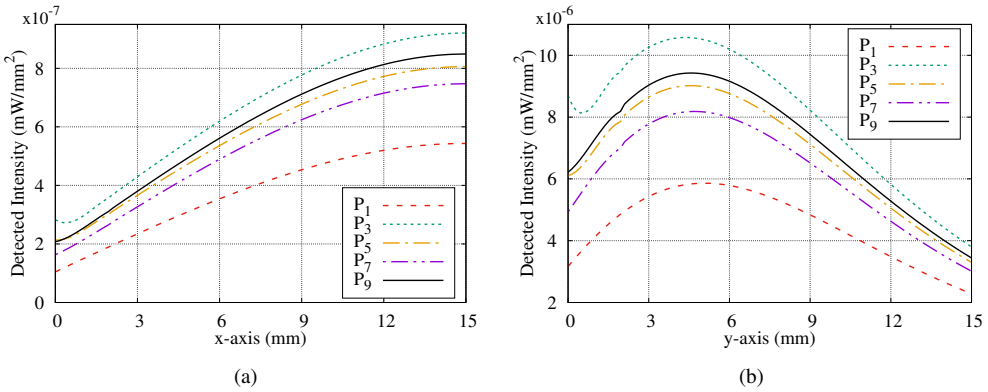

Fig. 5. Comparison of the P_L solutions for the detected photon intensity, calculated for source position A, in (a) for $y = 30$ mm, and (b) for $x = 0$ mm.

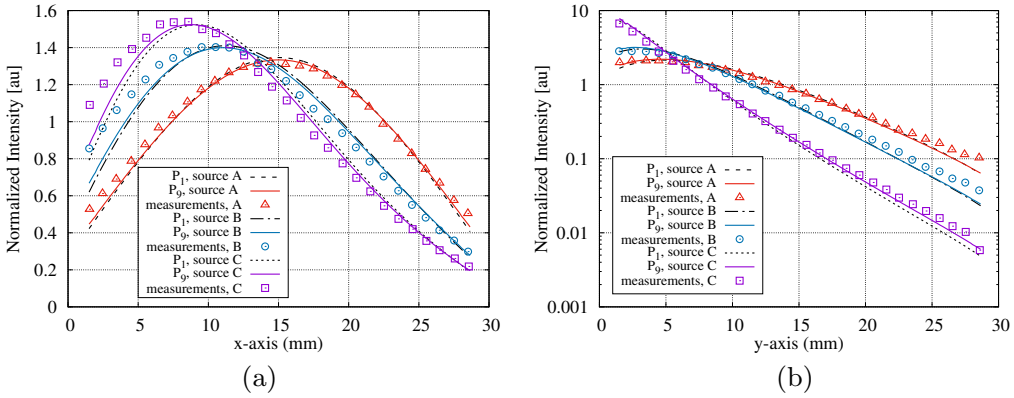

Fig. 6. Comparison of the normalized P_1 and P_9 transmitted photon intensity solutions with experimental data for the homogeneous phantom I, in (a) for $y = 30$ mm along the X-axis, and in (b) for $x = 0$ mm along the Y-axis. Calculations and data are generated for different source positions.

model in [29] describes a solution in two spatial dimensions and one angular coordinate (the azimuthal angle). On the other hand, the RTE (1) is a full model that depends on two angular variables; the average over the polar angle accounts for the factor $1/2$ that relates both results.

3.2.2. 2D heterogeneous phantom II

Now we consider the two-dimensional heterogeneous *phantom II* studied in [29]. The system is a $4\,\text{cm} \times 4\,\text{cm}$ square containing a void-like ring with an inner diameter of 2.8 cm and an outer diameter of 3.0 cm, as can be seen in Fig. 4 (right). A continuous wave source with a width of 0.1 cm is placed at three different locations along the X-axis (A at $x = 2.0\,\text{cm}$; B at $x = 1.2\,\text{cm}$ and C at $x = 0.4\,\text{cm}$).

The SHNC P_L numerical solutions for the normalized transmitted photon intensity are compared with 38 experimental data extracted from Fig. 7 of [29], the measurements were taken along the top side ($0 \leq x < 4\,\text{cm}$, $y = 4\,\text{cm}$) and the left side ($x = 0\,\text{cm}$, $0 \leq y \leq 4\,\text{cm}$) of the medium. The optical properties considered for the material of phantom I in Fig. 6 are now taken for the background medium of phantom II: $\mu_s' = 5.8\ \text{cm}^{-1}$, $\mu_a = 0.175\ \text{cm}^{-1}$ and $g = 0.8$. The

spatial discretization chosen for the medium is 40×40, showed in Fig. 4 (right). We have verified that no significant numerical improvements are achieved for a mesh with half node width.

We have evaluated the average error E between the P_7 numerical results and the experimental measurements, when the optical properties of the void-like ring are varied. The greatest changes in E are observed when the scattering coefficient is varied. Table 2 shows the error E for the P_7 calculations when $\mu_a = 0.06\,\mathrm{cm}^{-1}$ is fixed, $g = 0$ and μ_s is varied. It is observed that the error decreases consistently with the scattering parameter. We have not performed further reduction of μ_s because the resulting numerical linear problem becomes ill-conditioned and the convergence of the standard numerical methods used in their resolution gets worse.

Table 2. Average error E between the calculated P_7 and the measured normalized intensities along the top and the left sides of phantom II. Results are calculated for $\mu_a = 0.06\,\mathbf{cm}^{-1}$ and varying μ_s in the void-like region.

	Top side (X-axis, $y = 4$ cm)			Left side (Y-axis, $x = 0$ cm)		
μ_s (cm^{-1})	Source A	Source B	Source C	Source A	Source B	Source C
2.5	1.43	1.42	2.06	1.44	4.28	5.08
7.5	1.54	1.56	2.25	1.88	4.83	5.54
12.5	1.61	1.66	2.38	2.21	5.23	5.85
17.5	1.66	1.74	2.49	2.49	5.55	6.10
22.5	1.69	1.79	2.57	2.73	5.82	6.30

3.3. Time profile of a heterogeneous medium with an internal absorber region

We apply the spherical harmonics-nodal collocation method to study the photon propagation through a circular heterogeneous medium, consisting of two different regions with different absorption properties. This problem is based on one of the cases studied in [11]. The system consists of a circle of radius 15 mm enclosing in its center a small circular region of radius 1.5 mm, as can be seen in Fig 7 (a). The source and detectors are placed at the boundary of the outer circle. The optical parameters of the small circle are $\mu_a = 0.3\,\mathrm{mm}^{-1}$, scattering property $\mu_s = 2.5\,\mathrm{mm}^{-1}$ and $g = 0$. The same scattering coefficient is considered for the outer circle while in this region an anisotropy factor of $g = 0.8$ and an absorption coefficient of $\mu_a = 0.1\,\mathrm{mm}^{-1}$ are employed. An incident light pulse source having an intensity of 10^3 photons/mm^2 is applied for 2 ps at 0^o on the boundary.

For the numerical P_L calculations, we use a spatial discretization consisting of 2828 squared nodes with side length of 0.5 mm. The number of nodes has been chosen such that the relative percentage difference between the area of each circle and the area of the corresponding grid, is less than 1%. In our numerical calculations, the source extends in 2 nodes with a width of 1 mm, centered at the right half of the outer circle boundary (0^o). For this problem, reference P_L solutions were obtained using Crank-Nicolson scheme for the time discretization with 1516 time steps (a temporal discretization step of $\Delta t = 0.1$ s for $0 \leq t \leq 2$ s and $\Delta t = 0.5$ s for $2 \leq t \leq 750$ s). These reference solutions were compared with calculations obtained using 60 time steps, verifying that there are no significant changes in the P_L results and accurate results can be obtained with large time steps.

Fig. 7 (b) shows the time dependence of the detected photon current (6) at 90^o and 180^o from the source, calculated with P_1 or P_3 and P_7 approximations in each case. For the detector located at 90^o, we omit the P_1 solution because it is out of the graph scale (the maximum value of the P_1

current is 1.760×10^{-6} photons/mm^2 ps). The P_1 and P_7 solutions are compared in Fig. 7 at 180^o from the source and the P_3 result has been omitted in this case because it is indistinguishable from the P_7 curve.

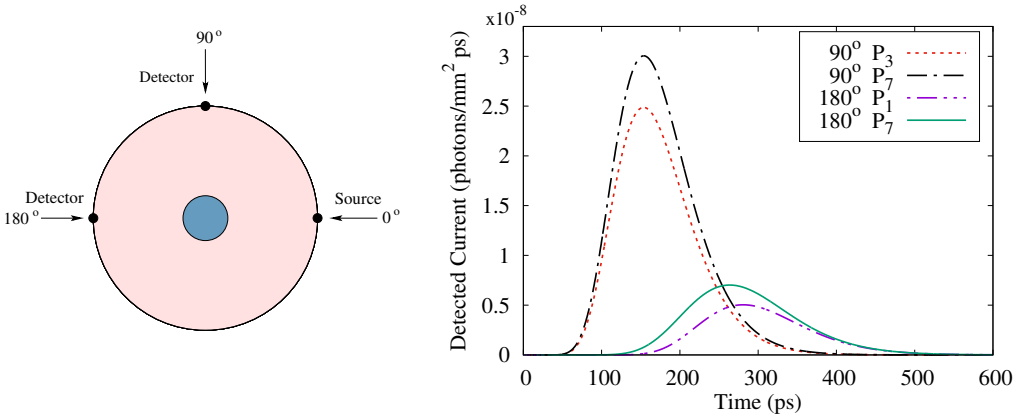

Fig. 7. (a) Configuration of the heterogeneous circular medium with the position of the source and detectors. (b) Time profile of photon current calculated with different P_L approximations, for detectors located at 90^o and 180^o.

As in [11], the greatest differences between the P_L results of the photon current occur in the region near the maximum values, although the time in which these peaks are reached varies slightly with the P_L approximation. In Table 3 we show the maximum values of the P_1, P_3 and P_7 detected photon currents at 180^o, when varying the absorption coefficient of the larger circle. The results in the Table show decrease in the peak current when absorption increases. We observe that the three P_L angular approximations show the same tendency when absorption is increased, although when $\mu_a \neq 0$, the P_3 and P_7 results are closer to each other than the P_1 solution. The relative difference between P_1 and P_7 values in Table 3 for $\mu_a = 0$ is 4.04%. This difference is greater when the absorption increases: 28.10% and 61.95% for $\mu_a = 0.1\,\text{mm}^{-1}$ and $\mu_a = 0.2\,\text{mm}^{-1}$, respectively.

Table 3. Maximum values of the current (photons/mm^2 ps) at 180^o from the source for the heterogeneous circular problem, for different values of μ_a in the outer circle

Cases	SHNC - Order of approximations		
μ_a (mm^{-1})	P_1	P_3	P_7
0.0	1.118×10^{-3}	1.158×10^{-3}	1.165×10^{-3}
0.1	5.126×10^{-9}	7.151×10^{-9}	7.130×10^{-9}
0.2	1.661×10^{-12}	4.388×10^{-12}	4.366×10^{-12}

Computations were carried out sequentially on an AMD Phenom 2.8GHz computer. The times required for single-core computations when considering 60 time steps are shown in Table 4 (in minutes) for the case with $\mu_a = 0.1\,\text{mm}^{-1}$ in the outer circle and $0 \leq t \leq 750\,\text{s}$.

Fig. 8 displays the P_7 photon intensity distribution into the medium, calculated at different moments after the 2 ps pulse source and with the same optical parameters used in Fig. 7 (b).

Table 4. SHNC P_L computation times for the $\mu_a = 0.1\,\mathrm{mm}^{-1}$ case, with 60 time steps and 2828 spatial nodes

SHNC order	CPU times (min)
P_1	2.20
P_3	30.83
P_7	261.94

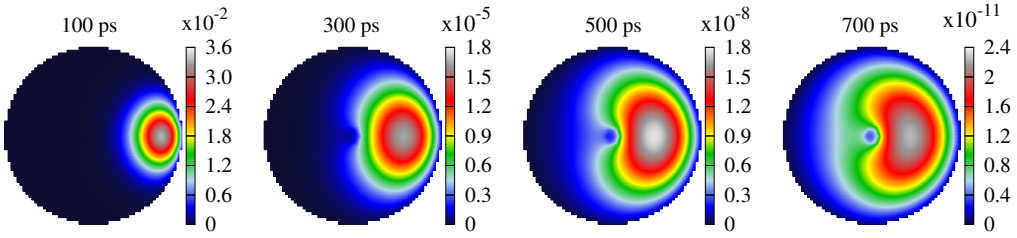

Fig. 8. Spatial distribution of the P_7 photon intensity in the heterogeneous circular medium at different time instants after the 2 ps light pulse.

4. CONCLUSIONS

We have adapted the spherical harmonics-nodal collocation method for time-dependent radiative transport problems, employing classical time-discretization schemes. The formalism is valid for absorbing media with anisotropic scattering and reflecting (Fresnel) boundary conditions, with external and/or internal sources. We allow that the physical properties of the media can change with time. The P_L approximation is carried out for arbitrary odd order L. The spatial discretization performed by a nodal collocation method is done on a rectangular mesh where the spatial variables are replaced by a finite sum of Legendre polynomials of arbitrary order M. This allows us to employ relatively large spatial nodes without losing accuracy in the computations. The adequate incorporation of Fresnel boundary conditions to the formalism has been fundamental for the correct predictions of the method.

We have performed some 1D and 2D numerical test calculations in scenarios inspired in optical tomography of biological tissues. We have compared our numerical P_L results with reference solutions in 1D cases with refractive index mismatching at the boundaries, and also when the external source is a highly anisotropic incident radiation. The agreement between our results and reference solutions has been confirmed for these cases. The P_L results have been tested with experimental measurements obtained from the literature, for a 2D homogeneous medium and a 2D heterogeneous medium containing a void-like ring. Also, we have studied the time profile of the P_L results for a 2D heterogeneous circular region with an internal absorber circle, showing the behavior of our solutions when the absorption in one of the regions is changed.

In problems where the requirements of the diffusion approximation are not satisfied, we have shown that the SHNC code gives satisfactory results employing high order P_L approximations. For these particular tests cases it is required at least P_5 or, even better, P_7 approximation, to accurately describe the anisotropies of the physical models.

In future works, our aim is to extend the formalism to non-equilibrium radiative transfer, where the radiative transfer equation is coupled to a material balance equation. Also, the extension of the method to the RTE for polarized beams is straightforward, with the scalar photon intensity replaced by the Stokes vector.

A. COMPUTATION OF THE RADIATION TRANSMITTED TO AN EXTERNAL DETECTOR

The computation of the integrals $\mathcal{I}_{c,s}(l,m)$ in Eq. (16) depends on the orientation of the boundary surface. For example, if $\mathbf{n} = (0,0,1)$ (positive Z-axis), $\alpha_r = \theta$, $\Omega_{\rm ap} = \{0 < \varphi < 2\pi,\ 0 < \theta < \alpha_i^{\max}\}$ (with $\sin\alpha_i^{\max} = n_0/n_m \sin\alpha_t^{\max}$), then

$$\begin{aligned}\mathcal{I}_c^{Z+}(l,m) &= \int_0^{2\pi} d\varphi \int_0^{\alpha_i^{\max}} \sin\theta\, d\theta\, [1 - R(\cos\theta)]\, \cos(m\varphi)\, P_l^m(\cos\theta) \\ &= 2\pi\delta_{m0} \int_{\eta_0}^{1} [1 - R(\eta)]\, P_l(\eta)\, d\eta\,, \qquad l = 0,1,\ldots,L\,,\ \ m = 0,\ldots,l\,, \quad (35)\end{aligned}$$

where $\eta_0 = \cos\alpha_i^{\max}$. Also, $\mathcal{I}_s^{Z+}(l,m) = 0$. In a similar way, for the positive X and Y axis, only the following integrals are non-zero:

$$\begin{aligned}&\mathcal{I}_c^{X+}(l,m) = 4\int_0^{\alpha_i^{\max}} d\varphi\, \cos(m\varphi) \int_0^{\eta_0} d\eta\, [1 - R(\cos\varphi\sqrt{1-\eta^2})] P_l^m(\eta)\,, \text{ when } l+m \text{ is even,} \\ &\mathcal{I}_c^{Y+}(l,m) = (-1)^k \mathcal{I}_c^{X+}(l,m)\,, \text{ when } m = 2k \text{ is even,} \\ &\mathcal{I}_s^{Y+}(l,m) = -(-1)^k \mathcal{I}_c^{X+}(l,m)\,, \text{ when } m = 2k-1 \text{ is odd,}\end{aligned}$$

where $\eta_0 = \sqrt{1 - \cos^2\alpha_i^{\max}/\cos^2\varphi}$. When $\mathbf{n}$ points to any of the three Cartesian negative axis, it can be shown that $\mathcal{I}_{c,s}^{-}(l,m) = (-1)^m \mathcal{I}_{c,s}^{+}(l,m)$.

Finally, the computation of Eq. (16) requires the knowledge of the coefficients $\{\xi_{lm}, \eta_{lm}\}$ with even index l, given by the vector X solution of the diffusive P_L equation (13), and also of the coefficients with odd index l, given by vector $\bar{X}$ that will be computed from Eq. (12) as a function of X. This will be done for each of the spatial nodes N_u^e where the nodal collocation approximation is applied. Then, for spatial node e (the superindex indicates that we take the values of the variables at this particular node)

$$\bar{X}^e(\mathbf{u}) = -D^e \sum_{j=1}^{3} \bar{M}_j \frac{1}{\Delta x_j^e} \frac{\partial X^e}{\partial u_j} + D^e\, \bar{\mathcal{S}}^e\,, \quad (36)$$

that requires, according to expansion (24), the computation of $\mathcal{P}'_k(u) = 2\sqrt{2k+1}\, P'_k(2u)$. This can be easily done from the recurrence $P'_{l+1} - P'_{l-1} = (2l+1)P_l$ [32]:

$$\mathcal{P}'_0 = 0\,, \quad \mathcal{P}'_1 = 2\sqrt{3}\,, \quad \mathcal{P}'_l = \sqrt{\frac{2l+1}{2l-3}}\, \mathcal{P}'_{l-2} + 2\sqrt{2l+1}\,\sqrt{2l-1}\mathcal{P}_{l-1}\,, \quad l = 2,3,\ldots$$

B. RECURRENCE RELATIONS FOR THE COEFFICIENTS OF THE LEGENDRE SERIES OF THE GAUSSIAN FUNCTION

The computation of the coefficients $T_{l\,=\text{odd}}$ in Eq. (33) requires the evaluation of the integrals

$$\mathcal{I}_l = \int_0^1 \exp\left[-\frac{(\eta-1)^2}{\epsilon^2}\right] P_l(\eta)\, d\eta\,. \quad (37)$$

If, when $l > 1$, we make use of the recurrence relations for Legendre polynomials [32]

$$\begin{aligned}&l\, P_l(x) = (2l-1)xP_{l-1}(x) - (l-1)P_{l-2}(x)\,, \\ &P'_{l+1}(x) - P'_{l-1}(x) = (2l+1)P_l(x)\,,\end{aligned} \quad (38)$$

and perform integration by parts, we obtain that, for $l = 2, 3, \ldots$,

$$\mathcal{I}_l = \frac{2l-1}{l}\mathcal{I}_{l-1} - \frac{l-1}{l}\mathcal{I}_{l-2} + \frac{\epsilon^2}{2}\frac{2l-1}{l}\mathcal{I}'_{l-1} - \frac{\epsilon^2}{2}\frac{2l-1}{l}\left(P_{l-1}(1) - \exp(-\epsilon^{-2})P_{l-1}(0)\right),$$

where $P_l(1) = 1$ and we have defined $\mathcal{I}'_l = \int_0^1 \exp[-(\eta-1)^2/\epsilon^2]P'_l(\eta)\,d\eta = \mathcal{I}'_{l-2} + (2l-1)\mathcal{I}_{l-1}$. In summary, we obtain the following recurrence relations:

$$\begin{aligned}
\mathcal{I}_0 &= \int_0^1 \exp\left[-\frac{(\eta-1)^2}{\epsilon^2}\right] d\eta = \epsilon\frac{\sqrt{\pi}}{2}\operatorname{erf}(\epsilon^{-1}), \qquad \text{where } \operatorname{erf}(x) = \frac{2}{\sqrt{\pi}}\int_0^x \exp(-t^2)\,dt,\\
\mathcal{I}_1 &= \int_0^1 \exp\left[-\frac{(\eta-1)^2}{\epsilon^2}\right] \eta\,d\eta = -\frac{\epsilon^2}{2}(1-\exp(-\epsilon^{-2})) + \epsilon\frac{\sqrt{\pi}}{2}\operatorname{erf}(\epsilon^{-1}),\\
\mathcal{I}'_0 &= \int_0^1 \exp\left[-\frac{(\eta-1)^2}{\epsilon^2}\right] P'_0(\eta)\,d\eta = 0, \qquad \mathcal{I}'_1 = \int_0^1 \exp\left[-\frac{(\eta-1)^2}{\epsilon^2}\right] P'_1(\eta)\,d\eta = \mathcal{I}_0, \quad (39)\\
\mathcal{I}_l &= \frac{2l-1}{l}\mathcal{I}_{l-1} - \frac{l-1}{l}\mathcal{I}_{l-2} + \frac{\epsilon^2}{2}\frac{2l-1}{l}\mathcal{I}'_{l-1} - \frac{\epsilon^2}{2}\frac{2l-1}{l}\left(1-\exp(-\epsilon^{-2})P_{l-1}(0)\right),\ l = 2, 3, \ldots,\\
\mathcal{I}'_l &= \mathcal{I}'_{l-2} + (2l-1)\mathcal{I}_{l-1}, \quad l = 2, 3, \ldots.
\end{aligned}$$

Finally, the values of $P_l(0)$ can be computed from the recurrences (38):

$$P_0(0) = 1, \quad P_1(0) = 0, \quad P_l(0) = -\frac{l-1}{l}P_{l-2}(0), \quad l = 2, 3, \ldots \qquad (40)$$

Acknowledgment

Partial support has been received by the Spanish Agencia Estatal de Investigación under project ENE2017-89029-P-AR. The authors express their gratitude to the anonymous reviewers for their suggestions and helpful comments.

References

1. B. Su and G. L. Olson, "An analytical benchmark for nonequilibrium radiative transfer in an isotropically scattering medium", Ann. Nucl. Energy **24**(13), 1035–1055 (1997).
2. M. F. Modest, *Radiative Heat Transfer* (Academic Press, 2013).
3. A. D. Klose and A. H. Hielscher, "Optical tomography with the equation of radiative transfer", Int. J. Numer. Method. H. **18**(3/4), 443–464 (2008).
4. E. E. Lewis and W. F. Miller, *Computational Methods of Neutron Transport* (John Wiley and Sons, New York, 1984).
5. M. R. J. Charest, C. P. T. Groth and Ö. L. Gülder, "Solution of the equation of radiative transfer using a Newton-Krylov approach and adaptive mesh refinement", J. Comp. Phys. **231**, 3023–3040 (2012).
6. R. Tapimo, H. T. T. Kamdem and D. Yemele, "Discrete spherical harmonics method for radiative transfer in scalar planar inhomogeneous atmosphere", J. Opt. Soc. Am. A **35**(7), 1081–1090 (2018).
7. B. Davison, "On the rate of convergence of the spherical harmonics method", Canad. J. Phys. **38**, 1526–1545 (1960).
8. K. M. Katika and L. Pilon, "Modified method of characteristics in transient radiation transfer", J. Quant. Spectrosc. Radiat. Transfer **98**, 220–237 (2006).
9. A. H. Hielscher, R. E. Alcouffe and R. L. Barbour, "Comparison of finite-difference transport and diffusion calculations for photon migration in homogeneous and heterogeneous tissues", Phys. Med. Biol. **43**, 1285–1302 (1998).
10. L. H. Liu and L. J. Liu, "Discontinuous finite element approach for transient radiative transfer equation", J. Heat Transfer **129**, 1069–1074 (2007).
11. E. D. Aydin, S. Katsimichas and C. R. E. de Oliveira, "Time-dependent diffusion and transport calculations using a finite-element-spherical harmonics method", J. Quant. Spectrosc. Radiat. Transfer **95**, 349–363 (2005).
12. J. Chen, M. Hillman and S. Chi, "Meshfree methods: progress made after 20 years", J. Eng. Mech. **143**(4), doi: 10.1061/(ASCE)EM.1943-7889.0001176 (2017).
13. Z. M. Tan and P. F. Hsu, "An Integral formulation of transient radiative transfer", J. Heat Transfer **123**, 466–475 (2001).
14. J. Spanier and E. M. Gelbard, *Monte Carlo principles and neutron transport problems* (Dover Publications, Mineloa, NY, 2008).
15. A. Hébert, "Development of the nodal collocation method for solving the neutron diffusion equation", Ann. Nucl. Energy **14**(10), 527–541 (1987).

16. M. Capilla, C. F. Talavera, D. Ginestar and G. Verdú, "A nodal collocation method for the calculation of the lambda modes of the P_L equations", Ann. Nucl. Energy **32**, 1825–1853 (2005).
17. M. Capilla, C. F. Talavera, D. Ginestar and G. Verdú, "Application of a nodal collocation approximation for the multidimensional P_L equations to the 3D Takeda benchmark problems", Ann. Nucl. Energy **40**, 1–13 (2012).
18. E. M. Gelbard, "Simplified Harmonics Equations and their Use in Shielding Problems", Technical Report WAPD-T-1182, Bettis Atomic Power Laboratory (1961).
19. A. W. Larsen, J. E. Morel and J. M. McGhee, "Asymptotic derivation of the multigroup P_1 and simplified P_N equations with anisotropic scattering", Nucl. Sci. Eng. **123**, 328–342 (1996).
20. D. I. Tomasević and E. W. Larsen, "The simplified P_2 approximation", Nucl. Sci. Eng. **122**, 309–325 (1996).
21. H. C. Van de Hulst, *Multiple Light Scattering*: *Tables, Formulas and Applications* (New York: Academic, 1980).
22. H. Greenspan, C. N. Kelber and D. Okrent, *Computing Methods in Reactor Physics* (Gordon & Breach Science Publishers, New York, 1968).
23. W. M. Stacey, *Nuclear Reactor Physics* (Wiley, New York, 2001).
24. R. Piessens, E. de Doncker-Kapenga, C. W. Überhuber and D. Kahaner, *QUADPACK: A subroutine package for automatic integration* (Springer-Verlag, 1983. ISBN 978-3-540-12553-2).
25. G. Verdú, D. Ginestar, V. Vidal and J. L. Muñoz-Cobo, "3D λ modes of the neutron diffusion equation", Ann. Nucl. Energy **21**(7), 405–421 (1994).
26. Y. Saad, "SPARSKIT: a basic tool kit for sparse matrix computations-Version 2", http://www-users.cs.umn.edu/~saad/software/SPARSKIT.
27. S. Balay, S. Abhyankar, M. Adams, J. Brown, P. Brune, K. Buschelman, L. Dalcin, V. Eijkhout, W. Gropp, D. Karpeyev, D. Kaushik, M. Knepley, L. C. McInnes, K. Rupp, B. Smith, S. Zampini, H. Zhang and H. Zhang, "PETSc Users Manual", Technical Report ANL-95/11 - Revision 3.7, Argonne National Laboratory (2016).
28. M. T. Capilla, C. F. Talavera, D. Ginestar and G. Verdú, "A study of the radiative transfer equation using a spherical harmonics-nodal collocation method", J. Quant. Spectrosc. Radiat. Transfer **189**, 25–36 (2017).
29. A. D. Klose, U. Netz, J. Beuthan and A. H. Hielscher, "Optical tomography using the time-independent equation of radiative transfer–Part 1: forward model", J. Quant. Spectrosc. Radiat. Transfer **72**, 691–713 (2002).
30. M. Franck, A. Klar, E. W. Larsen and S. Yasuda, "Time-dependent simplified P_N approximation to the equations of radiative transfer", J. Comput. Phys. **226**, 2289–2305 (2007).
31. R. E. Alcouffe, R. S. Baker, J. A. Dahl, S. A. Turner and R. Ward, "PARTISN: A Time-Dependent, Parallel Neutral Particle Transport Code System" Los Alamos National Laboratory, LA-UR-08-07258 (2008).
32. R. Courant and D. Hilbert D, *Methods of Mathematical Physics, Vol. I* (Wiley-Interscience, 1962).